Received: 29 November 2022 | Revised: 6 March 2023 | Accepted: 29 March 2023

DOI: 10.1002/jev2.12323

RESEARCH ARTICLE

Convection and extracellular matrix binding control interstitial transport of extracellular vesicles

Peter A. Sariano[1] | **Rachel R. Mizenko**[1] | **Venktesh S. Shirure**[1] | **Abigail K. Brandt**[1] | **Bryan B. Nguyen**[1] | **Cem Nesiri**[1] | **Bhupinder S. Shergill**[1] | **Terza Brostoff**[1,2] | **David M. Rocke**[1,3] | **Alexander D. Borowsky**[4] | **Randy P. Carney**[1] | **Steven C. George**[1]

[1]Department of Biomedical Engineering, University of California, Davis, California, USA

[2]Department of Pathology, University of California, San Diego, California, USA

[3]Department of Public Health Sciences, Division of Biostatistics, University of California, Davis, California, USA

[4]Department of Pathology and Laboratory Medicine, University of California, Davis, Sacramento, California, USA

Correspondence
Steven C. George, Department of Biomedical Engineering 451 E. Health Sciences Drive, room 2315 University of California, Davis, Davis, CA 95616, USA.
Email: scgeorge@ucdavis.edu

Funding information
National Institutes of Health, Grant/Award Numbers: F31 NS120590, R01 EB030410, R21 AI161041, UH3 HL141800, R01 CA241666; National Science Foundation, Grant/Award Number: Graduate Research Fellowship; Department of Biomedical Engineering and the College of Engineering at the University of California, Davis; ARCS Foundation Scholar Award

Abstract

Extracellular vesicles (EVs) influence a host of normal and pathophysiological processes in vivo. Compared to soluble mediators, EVs can traffic a wide range of proteins on their surface including extracellular matrix (ECM) binding proteins, and their large size (~30-150 nm) limits diffusion. We isolated EVs from the MCF10 series—a model human cell line of breast cancer progression—and demonstrated increasing presence of laminin-binding integrins $\alpha 3\beta 1$ and $\alpha 6\beta 1$ on the EVs as the malignant potential of the MCF10 cells increased. Transport of the EVs within a microfluidic device under controlled physiological interstitial flow (0.15-0.75 μm/s) demonstrated that convection was the dominant mechanism of transport. Binding of the EVs to the ECM enhanced the spatial concentration and gradient, which was mitigated by blocking integrins $\alpha 3\beta 1$ and $\alpha 6\beta 1$. Our studies demonstrate that convection and ECM binding are the dominant mechanisms controlling EV interstitial transport and should be leveraged in nanotherapeutic design.

KEYWORDS
diffusion, exosome, gradient, integrin binding, spatial concentration

1 | INTRODUCTION

Over the past decade it has become clear that small (~30-150 nm diameter) extracellular vesicles (EVs) represent a distinct and fundamental component of how neighbouring and distant cells and tissues communicate. The breadth of observations is impressive, including normal biological processes, such as cell migration (Kriebel et al., 2018; Sung & Weaver, 2017), differentiation (Hosseini et al., 2021; Yuan et al., 2021), and proliferation (Huang et al., 2019; Matsumoto et al., 2020), as well as pathological processes such as priming the metastatic niche in cancer (Becker et al., 2016). EVs are composite nanoparticles, secreted by cells, that are comprised of a lipid-based membrane surrounding an aqueous core. The membrane and core can each incorporate a wide

Randy P. Carney and Steven C. George contributed equally as co-senior authors

This is an open access article under the terms of the Creative Commons Attribution-NonCommercial License, which permits use, distribution and reproduction in any medium, provided the original work is properly cited and is not used for commercial purposes.
© 2023 The Authors. *Journal of Extracellular Vesicles* published by Wiley Periodicals, LLC on behalf of the International Society for Extracellular Vesicles.

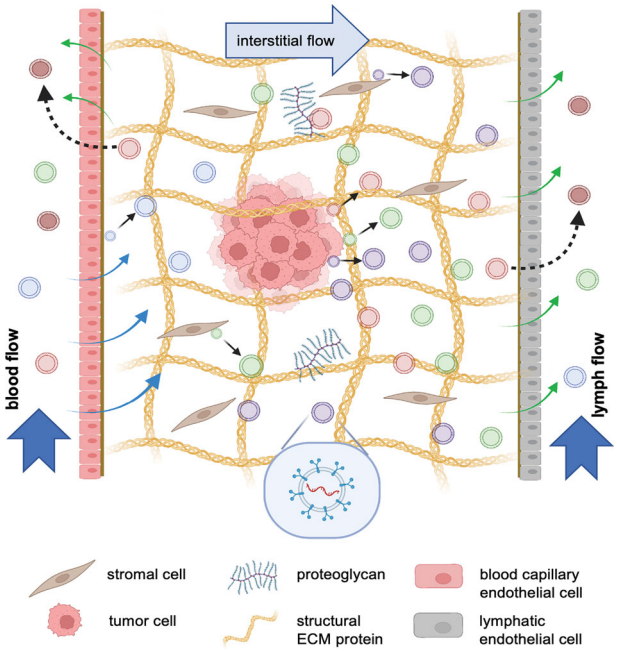

FIGURE 1 Extracellular vesicle transport and binding in the interstitium. A heterogeneous population of extracellular vesicles (EV) are secreted by all cell types (small black arrows), including tumor cells, and can directly enter the blood or lymphatic circulations or be transported by convection through the extracellular matrix by interstitial flow. Interstitial flow is generated as water leaks from the blood capillaries (blue arrows) into the interstitium. A small portion of the leak is reabsorbed near the venular end of the blood capillary (green arrows), and the remaining by the lymphatic capillaries (green arrows) generating a net interstitial flow from the blood capillaries to the lymphatic capillaries. As EVs are transported through the interstitium, they have the potential to bind (and release) to the ECM, thus impacting the population of EVs that are absorbed by the blood and lymphatic capillaries (black dashed arrows), and also establishing the spatial distribution in the interstitium of bound and free EVs. (constructed, in part, in BioRender).

range of biologically-active molecules (e.g., proteins, nucleic acids). These characteristics endow EVs with numerous desirable qualities (e.g., stability in circulating biofluids (Elsharkasy et al., 2020); relatively rapid cellular uptake (Bonsergent et al., 2021)) which might be leveraged in the design of nanotherapeutics. Despite the enormous potential of EVs as a nanotechnology, there are currently no FDA-approved EV formulations, and our fundamental understanding of their endogenous biology remains in its infancy.

While much work has been dedicated to characterizing the function of EVs in the tissue microenvironment, much less is known about their physical location, distribution, and concentration within the interstitium. The interstitial space broadly describes the tissue microenvironment between the blood and lymphatic microvasculature and is characterized by a porous extracellular matrix (ECM) and interstitial flow (fluid exits the capillary bed and is reabsorbed by blood capillaries and lymphatics) (Figure 1). Pore size is heterogeneous and depends on the tissue, but there is significant evidence, largely from electron microscopy in adipose, skin, and breast tissue, to suggest a wide range (50-5000 nm) capable of allowing relatively uninhibited transport of EVs (Loh & Choong, 2013; Provenzano et al., 2006; Raviraj et al., 2012; L. Wang et al., 2013). EVs are resident constituents of the ECM (Brown et al., 2018; Huleihel et al., 2016), and can influence ECM architecture and structure through aggrecanases, matrix metalloproteinases, elastase, and likely other matrix digesting proteases (Dolo et al., 1998; Genschmer et al., 2019; Lo Cicero et al., 2012; You et al., 2015). EVs also have the potential to be transported through the ECM by diffusion (Lenzini et al., 2020), but, due to their large size, the molecular diffusivity is orders of magnitude smaller compared to small molecules (e.g., the respiratory gases) for which diffusion is a primary mode of ECM transport. Furthermore, EVs also actively bind to collagen, laminin, and fibronectin via adhesion molecules (e.g., integrins) present on the surface of EV populations (Genschmer et al., 2019; Huleihel et al., 2016; Sung et al., 2015) (Figure 1). As such, convection and ECM binding are likely to control the rate of transport and the interstitial concentration of EVs. Despite the fact that interstitial flow is a fundamental feature of essentially all tissue microenvironments, and can profoundly impact the spatial distribution of soluble mediators (Shirure et al., 2017; Swartz & Lund, 2012), its role in manipulating and transporting EVs within the interstitium has been largely unexplored.

Here we characterized diffusion, convection, and binding of EVs derived from the MCF10 human breast cell line series in a microfluidic device under controlled flow conditions through a laminin-rich ECM. The MCF10 series (MCF10A, normal; MCF10DCIS, pre-malignant; MCF10CA1, malignant) is widely used in both in vitro and in vivo studies of breast cancer (Behbod et al., 2009; Bessette et al., 2015; Espina et al., 2010; Imbalzano et al., 2009), including several studies assessing EVs isolated from these parent cells (Chin et al., 2018; Jordan et al., 2020; Risha et al., 2020; Vu et al., 2019). Furthermore, there is relatively high expression of adhesion molecules on cancer derived EVs (Jimenez et al., 2019), and several proteomics studies have demonstrated

20013078, 2023, 4, Downloaded from https://isevjournals.onlinelibrary.wiley.com/doi/10.1002/jev2.12323 by Randy Carney - University Of California - Davis , Wiley Online Library on [29/08/2024]. See the Terms and Conditions (https://onlinelibrary.wiley.com/terms-and-conditions) on Wiley Online Library for rules of use; OA articles are governed by the applicable Creative Commons License

increasing presence of relevant integrins on EVs from increasingly malignant parent epithelium, including integrins $\alpha 3$, $\alpha 6$, and $\beta 1$ (Chin et al., 2018; Gangoda et al., 2017). We demonstrate from both experimental and computational methods that under physiologic flow conditions, convection (not diffusion) and binding control EV transport in a laminin-rich ECM; furthermore, concentration of bound EV and spatial gradients are exaggerated as malignant potential increases, and these observations are due, in part, to enhanced expression of integrins $\alpha 3$, $\alpha 6$, and $\beta 1$.

2 | MATERIALS AND METHODS

2.1 | Cell culture

The MCF10 breast cancer progression series (MCF10A, normal; MCF10DCIS, pre-malignant; MCF10CA1, malignant) was purchased from Karmanos Cancer Center, and sub-cultured according to advised protocols. Culture medium for MCF10A cells consisted of DMEM/F12 (Thermo Fisher Scientific), supplemented with 5% horse serum (Thermo Fisher Scientific), 1.05 mM $CaCl_2$ (Sigma-Aldrich), 20 ng/mL EGF (Thermo Fisher Scientific), 105 ng/mL cholera toxin (Millipore Sigma), 10 μg/mL insulin (Sigma), 0.5 μg/mL hydrocortisone (StemCell Technology). MCF10DCIS and MCF10CA1 culture medium consisted of DMEM/F12 supplemented with 5% horse serum and 1.05 mM $CaCl_2$.

2.2 | EV isolation

To prepare EV-depleted serum for culture media, serum-depleted horse serum was prepared by serial centrifugation. Serum was centrifuged for 300×g for 10 min at 4°C to remove live cells and large debris, 2000×g for 15 min at 4°C to remove dead cells and apoptotic bodies, 10,000×g for 30 min at 4°C to remove larger microvesicles, and finally spun via ultracentrifugation overnight at 120,000×g at 4°C. Absence of serum EVs was validated via nanoparticle tracking analysis (NTA) with the NanoSight LM10 (Malvern Panalytical Ltd.).

To isolate MCF10 series EVs, MCF10A, MCF10DCIS, and MCF10CA1 cells were loaded into 3 T-150 flasks each at a starting confluency of approximately 15% (1.5×10^6 MCF10A cells, 1.5×10^6 MCF10DCIS cells, 2×10^6 MCF10CA1 cells) and cultured for 24 h in non-EV depleted media. Following 24-h culture, flasks were triple rinsed with ample PBS + 1 mM $CaCl_2$ and 1 mM $MgCl_2$ (Thermo Fisher Scientific) to remove horse serum-derived EVs. 15 mL of EV-depleted serum media was added to each flask and cells were cultured for 72 h. Final cell concentration was observed following 72-h culture and was between 80% and 95% confluent. Initial seeding was optimized to prevent 100% confluence over the course of the 4-day culture.

Conditioned media was collected and subjected to increasing centrifugation spins (300×g for 10 min at 4°C, 2000×g for 15 min at 4°C, 10,000×g for 30 min at 4°C). 150,000 kDa Amicon filters (Millipore Sigma) were loaded with 15 mL of pre-spun conditioned media and spun at 4000×g for 45 min according to manufacturer protocols for crude EV purification. The EV-retentate was collected and filters were washed with MilliQ water. EVs for downstream imaging analysis were stained with 2 mM CellTrace Far Red (Thermo Fisher Scientific) and incubated for 2 h at 37°C (Morales-Kastresana et al., 2017).

Following incubation with CellTrace Far Red (CTFR), EVs were separated from excess dye as well as free proteins via size exclusion chromatography (SEC). An Izon Automatic Fraction Collector and $qEV_{Original}$ 35 nm SEC columns (Izon) were loaded with 1 mL of concentrated EV stock. EV-rich fractions one through four were collected (0.5 mL each) and utilized for downstream experiments, while fractions five through twelve were collected to serve as EV-free controls.

2.3 | Nanoparticle tracking analysis

EV samples were diluted 1:250 in 0.22 μm filtered MilliQ water, and 1 mL samples were added to a NanoSight LM10 (Malvern Panalytical Ltd) to characterize EV size and concentration. An automated syringe pump (Harvard Bioscience) provided consistent flow of EV sample across the field of view to provide multiple measurements. 3 × 30s videos were acquired per sample at camera level 13, and NanoSight NTA 3.1 software was utilized for analysis with detection threshold 3–4.

2.4 | Transmission electron microscopy (TEM)

EVs were fixed in 1% glutaraldehyde for 5 min. A 10 μL droplet of EV/glutaraldehyde mix was placed on parafilm and a copper formvar grid was floated, copper side down, on the droplet for 40 min. The grid was then dried on filter paper, moved to a 100 μL droplet of MilliQ water to wash, dried again, and moved to a 50 μL droplet of 0.2 um filtered 4% uranyl acetate for 8 min. Grids

20013078, 2023, 4, Downloaded from https://isevjournals.onlinelibrary.wiley.com/doi/10.1002/jev2.12323 by Randy Carney - University Of California - Davis , Wiley Online Library on [29/08/2024]. See the Terms and Conditions (https://onlinelibrary.wiley.com/terms-and-conditions) on Wiley Online Library for rules of use; OA articles are governed by the applicable Creative Commons License

were then dried again on filter paper and allowed to air dry for at least 10 min before imaging. Grids were imaged on a Talos FEI L120C TEM (Thermo Fisher Scientific) from 11,000× to 36,000× magnification.

2.5 | Single EV protein characterization-ExoView

An ExoView R100 (NanoView Biosciences) was utilized for individual EV immunofluorescent analysis. EVs were diluted to an initial concentration between 6.66E6-1.32E7 EV/mL and diluted 1:1 with incubation solution (NanoView Biosciences) according to manufacturer protocols. EV solutions were loaded onto EV-TETRA-C ExoView Kits (NanoView Biosciences) and prepared via an ExoView CW100 Chip Washer (NanoView Biosciences). Fluorescently conjugated integrin antibodies (1:400 AF488 anti-integrin β1, clone-TS2/16, BioLegend; 1:200 PE anti-integrin β1, clone-TS2/16, BioLegend; 1:400 AF647 anti-integrin β1, clone-TS2/16, BioLegend; 1:400 PE anti-integrin α3, clone-ASC-1, BioLegend; 1:400 AF488 anti-integrin α6, clone-GoH3; BioLegend) and ExoView tetraspanin kit antibodies (1:500 AF647 anti-CD63, clone-H5C6; 1:500 AF555 anti-CD81, clone-JS 81; 1:500 AF488 anti-CD9, clone-HI9a) were added at the appropriate steps during the incubation procedure. MIgG thresholds were selected at approximately the 75th percentile to reject the majority of non-specific binding. EV counts and integrin or tetraspanin colocalization was normalized to MigG counts. To assess the percentage of integrin positive EVs, EVs were probed with fluorescently labeled anti-tetraspanin antibodies to determine the number of tetraspanin positive EVs and separately with fluorescent anti-integrin antibodies to assess the number of integrin positive EVs. Equal numbers of EVs were loaded for both conditions.

2.6 | Western blot

EV pellets were lysed in RIPA lysis buffer (Millipore) containing protease inhibitor cocktail (Roche). Protein was quantified by BCA (Thermo Fisher). A total of 10 μg of protein per lane was loaded on an 8%–16% graded Tris-Glycine polyacrylamide gel and proteins were transferred to a 0.2 μm PVDF membrane (Life Technologies). Membranes were blocked in 5% milk (Bio-Rad) in tris-buffered saline with 0.05% Tween-20 (TBST) overnight at 4°C, and then incubated with primary antibody in blocking buffer at room temperature for 1 h. Antibodies were used as follows: rabbit anti-integrin β1 at 1:500 (Abcam), rabbit anti-integrin α3 at 1:1000, and rabbit anti-integrin α6 at 1:2000. Secondary anti-rabbit HRP was diluted at 1:5000 in block buffer and incubated at 1 h at room temperature with rocking (Cell Signaling). Proteins were visualized with Supersignal West Pico PLUS chemiluminescent substrate (Thermo Fisher) using a FluorChem E (Protein Simple).

2.7 | Microfluidic platform

The microfluidic device leveraged for diffusion, convection, and *in silico* experiments was previously developed in the lab (Shirure et al., 2017). This device consists of five parallel chambers communicating with other by diffusion and convection through small evenly spaced pores (Figure S1). The shape and dimensions of the pores create a capillary burst valve during loading limiting the hydrogel to the loading compartment (Cho et al., 2007; Moya et al., 2013). Microfluidic devices were fabricated with via soft-lithography with polydimethylsiloxane (PDMS). PDMS which was prepared by mixing a 10:1 ratio of Sylgard™ 184 silicone elastomer base and curing agent (Dow Corning) and pouring over SU-8 master molds. Cast-PDMS devices were bonded to glass coverslips (Thermo Fisher Scientific) via plasma treatment (Harrick Plasma).

200 μL pipette tips (Genesee Scientific) were added to fluidic ports at the end of chambers 1, 3a, and 3b, and filled with varying fluid volumes to establish controlled hydrostatic pressure heads. Differences in hydrostatic pressure head heights were leveraged to drive convective flow in in silico and in vitro convective flow experiments. Communication between chambers was established by structural micropores, which were previously optimized to avoid leakage of gels into neighboring chambers while also providing air-bubble free gel/fluid interfaces (pore width = 30 μm; pore length = 550 μm).

2.8 | In vitro diffusion experiments

To assess diffusion, CTFR stained MCF10 series EVs (1E9 EVs) were incubated with 1 mg/mL BSA (Thermo Fisher Scientific) for 15 min at 4°C to block nonspecific binding interactions. EVs were then incubated with a working solution of either 0.1 mM $CaCl_2$ and 1 mM $MgCl_2$, 1 mM MnCl2, 0.1 mM $CaCl_2$ and 1 mM $MgCl_2$ (all from Sigma-Aldrich) with a cocktail of functionally inhibitory integrin blocking antibodies (20 μg/mL anti-α3, clone-ASC-6, Millipore Sigma; 20 μg/mL anti-α6, clone-GoH3, Thermo Fisher Scientific; 50 μg/mL anti-β1, clone-mAb13, Millipore Sigma; 20 μg/mL anti-β4, clone-ASC-6, Millipore Sigma), or 1 mM $MnCl_2$ with the cocktail of functionally inhibitory integrin blocking antibodies. EV solutions were then mixed with laminin-rich ECM (Matrigel-GF Reduced; Corning) for a final laminin-rich ECM working concentration of 3 mg/mL and loaded

20013078, 2023, 4, Downloaded from https://isevjournals.onlinelibrary.wiley.com/doi/10.1002/jev2.12323 by Randy Carney - University Of California - Davis , Wiley Online Library on [29/08/2024]. See the Terms and Conditions (https://onlinelibrary.wiley.com/terms-and-conditions) on Wiley Online Library for rules of use; OA articles are governed by the applicable Creative Commons License

in chamber 2a or 2b (Figure S1). This concentration of Matrigel results in a matrix with a range of pore sizes similar to that present in vivo (50-5000 nm) (Zaman et al., 2006). Laminin-rich ECM was left to polymerize for 30 min at 37°C before FRAP imaging. Care was taken to prevent bulk convective fluid flow by ensuring loading heads were roughly equivalent, incubating for an additional 15 min at room temperature to allow time for fluid height equilibration, and leaving device chambers 1, 3a, and 3b devoid of fluid.

2.9 | Fluorescence recovery after photobleaching (FRAP)

FRAP was performed on an Olympus FV3000 laser scanning confocal microscope (Olympus) via a 20× objective with 3× digital zoom and captured by high sensitivity-spectral detector. FRAP images were acquired every 240 ms over the course of 5 min with a 100% laser excitation pulse after the first four frames to generate a circular 18 μm diameter bleach spot. Laser power was tuned to ensure that the final non-bleached background fluorescence was within 15% of the initial non-bleached background fluorescence on average.

The underlying pseudo first order kinetic equation describing EV interactions with the ECM can be described by:

$$EV + B \underset{k_{off}}{\overset{k_{on}}{\rightleftarrows}} EVB \tag{1}$$

where EV is the concentration of free EVs, B is the concentration of binding sites within the matrix, and EVB is the concentration of matrix-bound EVs. Initial concentrations of each species as well as forward (k_{on}) and reverse (k_{off}) rate constants determine final steady state concentrations of each species. The ratio of k_{off}/k_{on} provides the dissociation constant, K_d.

Raw FRAP data was analyzed in FIJI using a standard analysis pipeline. In brief, the "create profile" plugin (Unruh) was implemented to generate average fluorescent intensity spectrum curves over the full image stack. ROIs were generated for the bleach spot as well as a control ROI for the background fluorescence. The bleach spot fluorescent spectrum was normalized to a function fit to the background fluorescence ROI to control for photobleaching. Spectrum data was exported to MATLAB for further analysis. To perform fits, background-normalized spectrum data was normalized to fall within 0 and 1 by setting the mean value pre-bleach equal to 1 and the minimum value post-bleach equal to 0. A progressive sliding window was utilized to average timepoints in order to smooth the curves and to prevent biased overfitting of later timepoints. Sliding window conditions were as follows: T = 0-0.72s (Pre-bleach)—no averaging; T = 0.96-29.76s—averaged 2 points; T = 30.76-44.4s—averaged 5 points; T = 46.8-58.8s—averaged 10 points; T = 62.4-66s—averaged 15 points; T = 70.8-299.76s—averaged 20 points. Log space parameter arrays with 50 values were generated to screen the three fitting parameters: D (1E-13 → 1E-11), k^*_{on} (1E-7 → 1E-2), and K_d (1E-6 → 1E-1).

FRAP curve fitting procedures followed the general methodology previously described in detail to fit experimental data with pseudo first order kinetics (Equation 1). The following fitting equation was applied to the experimental FRAP recovery curves (Sprague et al., 2004):

$$\overline{frap}\ (p) = \frac{1}{p} - \frac{F_{eq}}{p}(1 - 2K_1\,(qw)\,I_1\,(qw) * \left(1 + \frac{k^*_{on}}{p + (K_d * k_{on})}\right) - \left(\frac{C_{eq}}{p + (K_d * k_{on})}\right) \tag{2}$$

where,

$$k^*_{on} = k_{on} * B_{eq} \tag{3}$$

$$F_{eq} = \frac{(K_d * k_{on})}{k^*_{on} + (K_d * k_{on})} \tag{4}$$

$$C_{eq} = \frac{k^*_{on}}{k^*_{on} + (K_d * k_{on})} \tag{5}$$

20013078, 2023, 4, Downloaded from https://isevjournals.onlinelibrary.wiley.com/doi/10.1002/jev2.12323 by Randy Carney - University Of California - Davis , Wiley Online Library on [29/08/2024]. See the Terms and Conditions (https://onlinelibrary.wiley.com/terms-and-conditions) on Wiley Online Library for rules of use; OA articles are governed by the applicable Creative Commons License

$$q = \sqrt{\left(\frac{p}{D}\right) * \left(1 + \frac{k^*_{on}}{p + (K_d * k_{on})}\right)} \quad (6)$$

where $\overline{frap}(p)$ is the average of the Laplace transform of the fluorescent intensity within the bleach spot, p is the Laplace variable that inverts to yield time, I_1 and K_1 are modified Bessel functions of the first and second kind respectively, w is the bleach spot radius, B_{eq} is the equilibrium concentration of binding sites, and D is the EV free diffusion coefficient. The numerical inversion of this function was performed via the "invlap.m" routine.

Fitting for exact values of k^*_{on} and k_{off} from fluorescence recovery curves is difficult due to the long relatively flat trough observed when plotting the minimized sum of squares of the residual (SSR) as a function of k^*_{on} and k_{off}. In other words, multiple combinations of k^*_{on} and k_{off} produce similar SSR, thus rendering it impossible to uniquely identify the individual binding parameters. The solution is to simply fit for the ratio of two, or K_d ($K_d = k_{off}/k_{on}$) (Figure S2). A matrix of $50 \times 50 \times 50$ curve libraries was generated by importing each combination of D, k^*_{on}, and K_d fitting parameters. A sum of squares approach was applied to minimize the error between library curves and experimental data. Preliminary best-fit parameters were extracted from the best fit curve.

To refine the fitting procedure, the MATLAB routine "fitnlm," was applied for higher accuracy fitting of k^*_{on} and K_d. D was constrained to the value determined through the first sum of squares residual estimation to reduce the burden on the fitting process and risk of overfitting the data. The "fitnlm" routine used the Levenberg-Marquardt nonlinear least squares algorithm. Resulting refined-fit parameters for k_{on} (k^*_{on}/B_{eq}) and K_d are presented in results, although the difference between the initial sum of squares fit and the refined fit were negligible.

2.10 | Finite element simulations (in silico experiments)

Computational finite element simulations were performed using COMSOL Multiphysics™ 5.2a software. The convection–diffusion equations of mass and momentum transport were solved to find flow velocities and spatial concentration profiles of EVs, binding sites, and bound EVs. The Free and Porous Media Flow module was used to model fluid through the porous ECM, and Transport of Diluted Species Modules were implemented to track transport of each species. Chemistry modules were added to capture the relationship between EVs and binding sites (Equation 1). 2D solutions were generated assuming incompressible, single-phase, laminar flow with no-slip boundary conditions applied to all surfaces with the exception of terminal port inlets and outlets (ends of chambers 1–3). EVs were modeled as a dilute, dissolved species which neglected physiologic drag and interactions with matrix porosity. Binding sites and bound EVs were modeled as effectively immobile with D= 1E-16 m^2/s. Baseline modeling parameters (Suppl. Table 1) were used unless otherwise specified. Note that the concentration of binding sites in a laminin-rich ECM is nearly five orders of magnitude higher than a typical concentration of EVs; as such, binding sites are in excess and the spatial concentration will be independent of EV concentration in the physiological range. Additional parameter values were: dynamic viscosity of water at 25°C = 0.89 cP; density of water at 25°C = 1000 kg/m^3; porosity of matrix = 0.99%. Various parameter and time sweeps were performed, and parameter values were tested iteratively along with in vitro experiments.

2.11 | In vitro interstitial flow experiments

Identical microfluidic devices as those used in FRAP experiments were utilized for convective flow experiments. CTFR-stained EVs were prepared as described above but were not embedded in laminin-rich ECM. Rather, laminin-rich ECM was prepared at 3 mg/mL and loaded into chambers 2a and 2b. Following a 30-minute incubation at 37°C, warmed PBS was added to minimize temperature shock to the hydrogel. The PBS was added to chambers 1, 3a, and 3b to establish hydrostatic pressure heads and convective flow from chamber 1 outwards across the matrix-filled chambers 2a and 2b towards fluidic chambers 3a and 3b. Devices were then allowed to equilibrate to room temperature over the next 30 min. To initiate fluid flow for convective flow experiments the following fluid volumes were added to 200 μL pipette tips to establish hydrostatic pressure heads: Chamber 1: Inlet-35 μL, Outlet-30 μL; Chamber 2a,b: filled with laminin-rich ECM, no additional pressure head was applied; Chamber 3a,b: Inlet-15 μL, Outlet-10 μL . Pressure heads were selected to ensure symmetry from the middle of chamber 1 outwards to fluidic chambers 3a and 3b.

40 kDa FITC dextran (Sigma-Aldrich) was added to EV solutions to serve as a control for fluid flow. EV and dextran flows were visualized via an Olympus FV3000 confocal microscope (Olympus) with a 10x objective using 647 and 488 nm lasers and captured by high sensitivity-spectral detectors to maximize capture of the EV fluorescent signal. Dextran velocity was calculated using iterative in vitro experiments and finite element modeling. In brief, displacements of dextran fluorescence over time were compared between in vitro and computational models. In silico parameter sweeps of ECM permeability provided associated

20013078, 2023, 4, Downloaded from https://isevjournals.onlinelibrary.wiley.com/doi/10.1002/jev2.12323 by Randy Carney - University Of California - Davis , Wiley Online Library on [29/08/2024]. See the Terms and Conditions (https://onlinelibrary.wiley.com/terms-and-conditions) on Wiley Online Library for rules of use; OA articles are governed by the applicable Creative Commons License

interstitial flow velocity values. Curves were generated to plot ECM permeability versus dextran displacement and interstitial fluid velocity versus ECM permeability. In vitro dextran displacement was plotted along these curves to identify interstitial flow velocity.

To assess EV convective flow and accumulation in the matrix, the following solutions were added to each device chamber via the same methodology and volumes indicated above: Chamber 1: EV (3×10 (Bonsergent et al., 2021) total EVs at a concentration of 4.6×10 (Becker et al., 2016) EV/μL) + 40 kDa dextran + treatment condition + PBS; Chamber 2a,b: filled with laminin-rich ECM; Chamber 3a,b: PBS. EV treatment conditions used the same concentrations of blocking antibodies described in diffusion experiments. 5 mM EDTA (Thermo Fisher Scientific) and RPMI 1640 were added for additional treatment conditions. Control experiments used fluorescent nanobeads (26 nm and 100 nm diameter; Thermo Scientific) rather than EVs to assess transport of a similarly sized, non-binding species.

Images were acquired at 1.08 s intervals over the first 10 min of flow. After 30 min of flow, images of the full device were acquired as a terminal endpoint. Data for convective flow experiments was analyzed in FIJI. Fluorescent intensity line profiles were generated to show EV concentration gradients across laminin-rich ECM chambers. Multiple ports from each device were measured, but analysis was limited to ports with flow velocities within a binned range: $0.15\ \mu\text{m/sec} \leq v \leq 0.75\ \mu\text{m/sec}$. Binning was performed to exclude ports with negligible flow as well as those with rapid flow caused by degraded laminin-rich ECM. The majority of ports were within the binned range.

2.12 | Statistical analysis and figure generation

The majority of experimental conditions were performed in triplicate at minimum. PRISM 9.2 was utilized for statistical analysis and generation of graphs. One-way ANOVA tests with a p-value < 0.05 and Tukey-Post hoc tests were employed when comparing three or more conditions, while student t-tests with a p-value < 0.05 were used to show significance when comparing only two conditions.

3 | RESULTS AND DISCUSSION

3.1 | EV features during malignant progression

We first isolated and characterized EVs from each line of the MCF10 series using NTA and TEM. EV size distributions (Figure 2a) were consistent with reported features, with most measured particles within the expected range <150 nm. EVs secreted per cell increased more than two-fold as the malignant potential of the cell line increased (Figure 2b). This result is consistent with observations demonstrating that EV secretion is often increased in cancerous cells due to signaling dysregulation (Kilinc et al., 2021) or microenvironmental factors such as acidic pH or hypoxia (Whiteside, 2016). EV size distribution was confirmed by TEM, with most demonstrating the characteristic cup-shaped morphology caused by dehydration and rupture of hydrated particles during TEM preparation (Figure 2c).

Using a dual antibody capture immunofluorescence technique (ExoView), we confirmed that EVs from all three cell lines express common tetraspanin markers (CD9, CD63, and CD81) enriched on cell-released EVs (Figure S3a). We also observed significant EV heterogeneity in tetraspanin presence across the MCF10 series which supports the observation that EVs from distinct cell sources can carry markedly different protein profiles (Garia-Martin et al., 2022; Mizenko et al., 2021), and that these profiles can transform with malignancy.

We next assessed integrin expression on the EVs. EV samples isolated from each cell line were immobilized (ExoView) and probed for laminin-binding integrins $\alpha 3$, $\alpha 6$, and $\beta 1$. Integrin positive EVs were determined by thresholding against the MIgG negative control. Comparison across the lines revealed significantly increased expression of all three integrins on MCF10CA1 EVs compared to normal or pre-malignant MCF10A or MCF10DCIS EVs (Figure 2d). There was no significant difference between MCF10A and MCF10DCIS EVs. When compared to the total population of EVs expressing at least one tetraspanin, the percentage of EVs expressing integrins $\alpha 3$, $\alpha 6$, and $\beta 1$ increased by approximately an order of magnitude from MCF10A (1%–2%) and MCF10DCIS (5%–6%) to MCF10CA1 (58%–62%) (Figure 2d and Suppl. Table 2). This trend was confirmed by Western blot (Figure S4).

Integrins require dimerization of α and β subunits to effectively bind ligand targets (Takada et al., 2007), which prompted analysis of the colocalization of integrins $\alpha 3$, $\alpha 6$, and $\beta 1$ on individual EVs. The presence of colocalized integrins on individual EVs increased two to four-fold with increasing parent cell malignancy for both $\alpha 3\beta 1$ and $\alpha 6\beta 1$ integrin pairs (Suppl. Table 3). The significant increase in the expression of integrins on EVs with malignant potential is consistent with previous reports demonstrating increased integrin expression on EVs from malignant cells (Chin et al., 2018; Gangoda et al., 2017), and is also consistent with the critical role for integrins in phenotypic features of metastatic tumors cells such as cell migration (Ganguly et al., 2013).

20013078, 2023, 4, Downloaded from https://isevjournals.onlinelibrary.wiley.com/doi/10.1002/jev2.12323 by Randy Carney - University Of California - Davis , Wiley Online Library on [29/08/2024]. See the Terms and Conditions (https://onlinelibrary.wiley.com/terms-and-conditions) on Wiley Online Library for rules of use; OA articles are governed by the applicable Creative Commons License

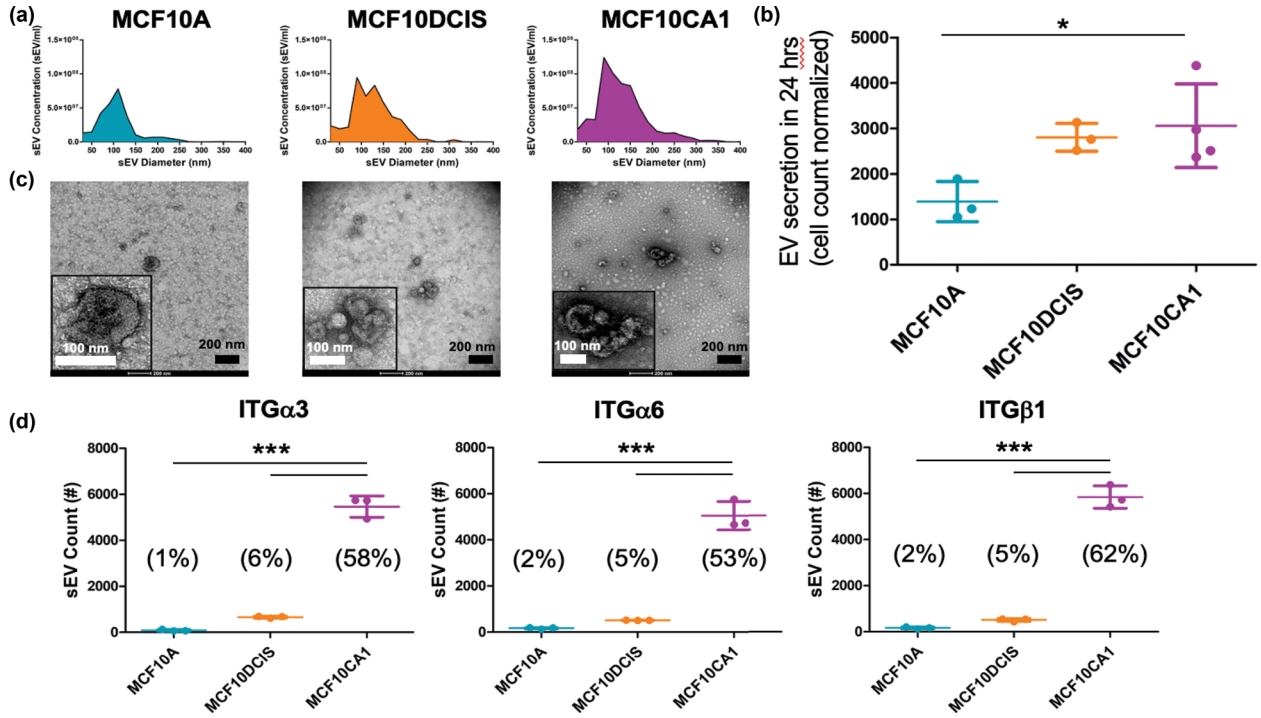

FIGURE 2 Isolation and characterization of EVs. (a) Nanoparticle tracking analysis (NTA) revealed expected EV size distribution and adequate concentration for in vitro studies as well as (b) increasing secretion with malignancy when normalized by cell number. (c) Transmission electron microscopy (TEM) demonstrated sufficient EV concentration and a characteristic cup-shape morphology. (d) Loading the same concentration of EVs revealed increasing expression of integrin $\alpha 3$, $\alpha 6$, and $\beta 1$ with parent cell malignancy by ExoView analysis. Percentage integrin positive of all tetraspanin positive EVs is shown in parentheses. $^{*}p = 0.0319$; $^{***}p < 0.0001$; One-way ANOVA, Tukey post-hoc.

Finally, combined with the significant increase in the absolute numbers of EVs shed by the MCF10CA1 cells (Figure 2b), our result suggests the potential for a dramatic increase in the number of bound EVs in the ECM of a malignant breast cancer.

3.2 | EV diffusive transport and binding

We next assessed the functional consequence of integrin expression on the EVs by characterizing the diffusivity and binding rates to a laminin-rich ECM using FRAP. FRAP analysis affords the ability to not only measure EV diffusion in bulk (i.e., molecular diffusivity), but also to derive kinetic binding parameters including forward (k_{on}), reverse (k_{off}), and equilibrium K_d (k_{off}/k_{on}) rate constants. We modelled the process of ECM binding as a pseudo first order process, $EV + B \overset{K_d}{\leftrightarrow} EVB$, where B is the concentration of binding sites and is considered in excess, and EVB is maxtrix-bound EVs. The kinetic parameters can be determined from the shape of the fluorescence recovery profile following photobleaching (Figure S5a) using non-linear regression of a diffusion-reaction model (Sprague et al., 2004). In addition to the diffusivity and kinetic binding parameters, the asymptotic level reached by FRAP curves is indicative of a bleached immobile fraction as well as the unbleached freely diffusing mobile fraction (Figure S5a).

The FRAP methodology and the analysis pipeline were first validated by performing bleaching experiments with 40 kDa and 150 kDa dextran (Figure S5b,c). We used a 3 mg/mL laminin-rich ECM (Matrigel-GF Reduced; Corning) that produces a matrix with comparable pore size range as that present in vivo (Zaman et al., 2006). The fluorescent signal from the dextrans recovered to nearly baseline, thus reflecting the expected lack of binding to matrix (no immobile fraction). The diffusivity of the 40 kDa and 150 kDa dextran were extracted from the fitted recovery curves (1.6×10^{-11} m^2/s and 0.94×10^{-11} m^2/s, respectively), and were ~40% of the theoretically estimated (Stokes-Einstein) (Rossi & Bianchi, 1961) diffusion coefficient in water (3.5×10^{-11} m^2/s and 2.6×10^{-11} m^2/s, respectively); thus consistent with diffusion in tissue-like hydrogels (George et al., 1996).

For integrins to form heterodimer pairs, divalent cations such as Ca^{2+} or Mg^{2+} are necessary to stabilize the interaction, and Mn^{2+} can be used to lock the integrins in a high affinity-binding state. As such, we modelled a low, intermediate, and high affinity integrin binding state of the EVs using either EDTA to chelate free cations or functionally-validated blocking antibodies ($\alpha 3$, $\alpha 6$, $\beta 1$, and $\beta 4$), $CaCl_2 + MgCl_2$, or $MnCl_2$, respectively. The fluorescence recovery curves for each of the cell lines and treatment conditions were then fit for k^*_{on} (product of k_{on} and the concentration of binding sites), K_d, and D, then combined, averaged,

20013078, 2023, 4, Downloaded from https://isevjournals.onlinelibrary.wiley.com/doi/10.1002/jev2.12323 by Randy Carney - University Of California - Davis , Wiley Online Library on [29/08/2024]. See the Terms and Conditions (https://onlinelibrary.wiley.com/terms-and-conditions) on Wiley Online Library for rules of use; OA articles are governed by the applicable Creative Commons License

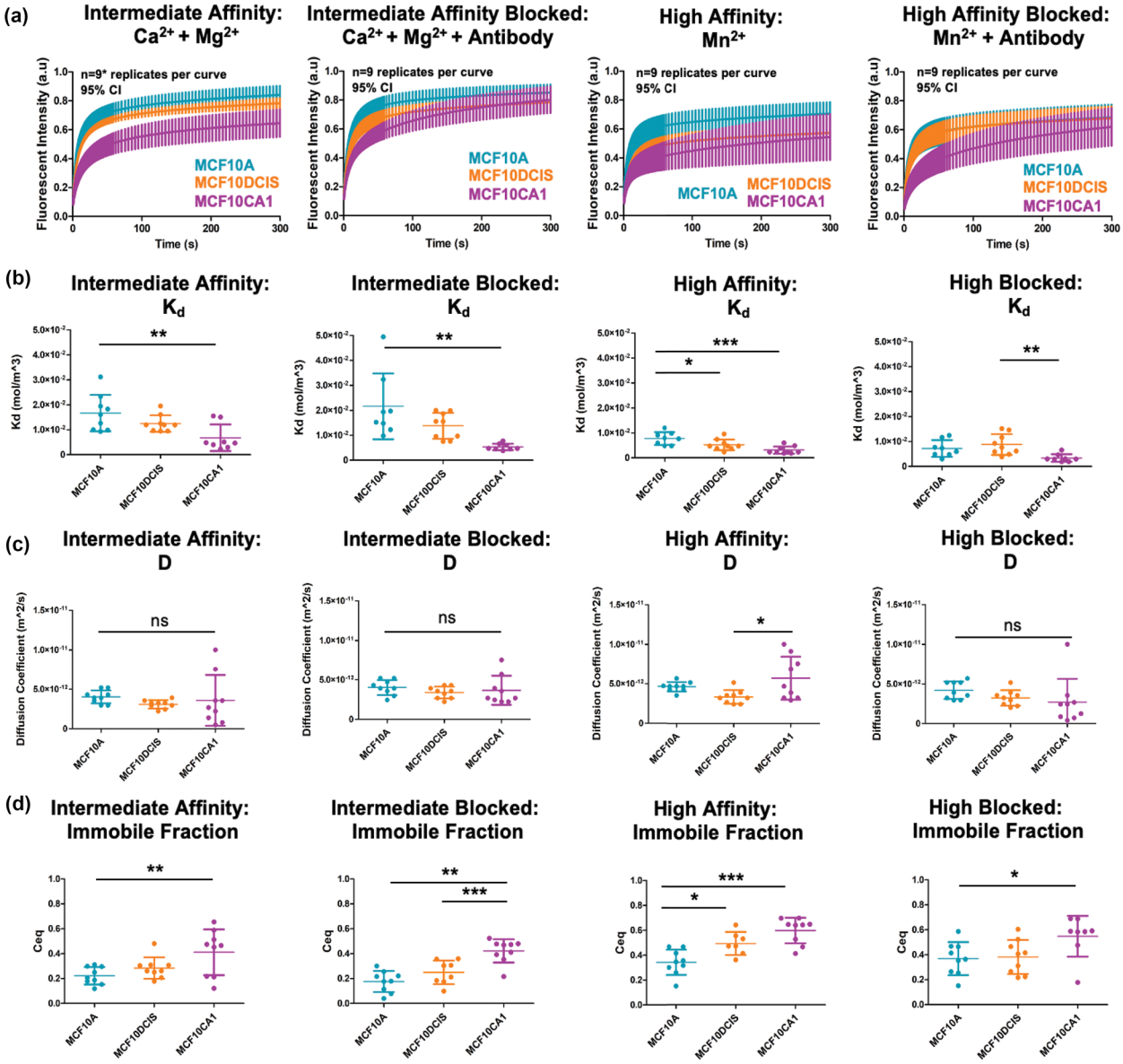

FIGURE 3 EV matrix binding is impacted by parent cell malignancy. (a) FRAP recovery fitted curves were consistently slower and lower for malignant MCF10CA1 EVs across all treatment conditions, followed by MCF10DCIS and MCF10A EVs. Recoveries generally appeared to display asymptotic behaviour by t = 300 sec. Error bars = 95% CI; $n = 9$ replicates per curve; $n^* = 8$ replicates for MCF10CA1 curve. (b) Fitted K_d parameter was consistent with behaviour in FRAP curves. MCF10CA1 EVs exhibited lowest K_d values, indicating the highest levels of EV binding to the matrix. (c) Molecular diffusivity was broadly independent of cell line or treatment condition. (d) The bound fraction (Ceq) was assessed for each integrin binding state. Highest EV binding fractions were observed with MCF10CA1 EVs in all conditions compared to EVs from MCF10A and MCF10DCIS. One-way Anova, Tukey post-hoc. $^*p < 0.05$, $^{**}p < 0.01$, $^{***}p < 0.001$; One-way ANOVA, Tukey post-hoc.

and plotted with 95% confidence intervals. For each condition, EVs isolated from MCF10CA1 exhibited slower initial recoveries and a lower plateau, consistent with ECM binding (Figure 3a). This observation was followed by MCF10DCIS EVs which shared 95% confidence intervals with MCF10A EVs at most time points.

We next fitted for the values of K_d and D for each of the curves to better understand the mechanism leading to the altered fluorescence recovery curves. EVs from the MCF10CA1 line consistently exhibited the lowest K_d across all conditions (Figure 3b). Because the biogenesis of EVs is only partially understood, we chose to limit integrin function using blocking antibodies rather than knocking down integrin expression in the parent cells, which could impact the number or character of EVs released. Integrin blocking had a minimal impact on K_d. This may be due to several possibilities: (1) the relatively small fraction of EVs that express $\alpha 3$, $\alpha 6$, and $\beta 1$ (for MCF10A and MCF10DCIS; Suppl. Tables 2 and 3); (2) k_{on} of other potential binding proteins (e.g., other integrins) are similar to $\alpha 3$, $\alpha 6$, $\beta 1$ under stagnant or no flow conditions; or 3) the overall fraction of total binding proteins that $\alpha 3$, $\alpha 6$, $\beta 1$ represents is relatively small. Of note is that blocking antibodies should not impact k_{off}. In contrast, D was not

20013078, 2023, 4, Downloaded from https://isevjournals.onlinelibrary.wiley.com/doi/10.1002/jev2.12323 by Randy Carney - University Of California - Davis , Wiley Online Library on [29/08/2024]. See the Terms and Conditions (https://onlinelibrary.wiley.com/terms-and-conditions) on Wiley Online Library for rules of use; OA articles are governed by the applicable Creative Commons License

impacted by cell line and integrin activation conditions with the exception of a small increase in MCF10CA1 in the high affinity condition (Figure 3c). The mean value for D (3.80×10^{-12} m^2/s) is consistent with previous estimates using nanoparticle tracking (Lenzini et al., 2020), and is within the range of theoretical values (3.4-17 $\times 10^{-12}$ m^2/s) of a sphere in water with a mean diameter ranging from 30 to 150 nm. Comparing the immobile, bound EV fraction (C_{eq}) for each condition (Figure 3d) resulted in similar trends to K_d. In other words, the increasing immobile fraction of EVs observed with increasing malignant potential is consistent with enhanced binding (lower K_d) to the ECM. The enhanced binding could be due to either a reduced k_{off}, an enhanced k_{on}, or a combination. A near constant value of D for the EVs across cell lines is consistent with Stokes-Einstein theory and the characterization of the free diffusion of EVs from each cell line, which demonstrate a similar size distribution (Figure 2).

3.3 | In silico model of EV convective transport and binding

With properties of EV diffusion and binding now characterized, we next investigated the role of physiological interstitial flow (convection) on the transport of EV in a laminin-rich ECM using a finite element computational model (COMSOL). The geometry of a previously described microfluidic device (Hwang et al., 2019; Shirure et al., 2017) was imported into COMSOL (Figure S1). The microfluidic device consists of five parallel chambers that can communicate by diffusion and convection through a series of small evenly dispersed pores. The pressure distribution and porosity create a physiological interstitial flow from the central chamber outwards through hydrogels loaded in the adjacent compartments. All modeling parameters were gathered from the literature or determined experimentally through iterative in vitro-*in silico* experiments (Suppl. Table 2).

We first demonstrated that physiological flow (velocity, range 0.1-10 μm/s) could be achieved using three different hydrostatic head pressure heads (5.5, 8.8, and 12.5 mm). These pressure heads produced mean interstitial flow velocities of 0.5, 0.75, and 1 μm/s, respectively, along the centerline between opposing pores across the interstitial microfluidic channel (Figure 4a). To assess the impact of convection on bound and free concentration of EVs, we introduced a constant concentration of EVs in the microfluidic line adjacent to the interstitial channel on the high-pressure side to allow EVs to enter the interstitial channel by convection. We considered no binding, intermediate (K_d of MCF10A in the presence of $MgCl_2$ and $CaCl_2$), and high (K_d of MCF10CA1 in presence of $MnCl_2$) (Suppl. Table 1). Across all integrin binding states and initial binding site concentrations, occupancy of binding sites was negligible, consistent with the fact that the binding site concentration was calculated to be several orders of magnitude higher than EV influx concentration. EV accumulation in the interstitial compartment increased with increasing EV binding affinity (Figure 4b). Concentration gradients between opposing pores in the interstitial channel were evident, but very small in magnitude, in both free and bound EV species (Figure 4c). Faster interstitial flow velocities flattened free and bound gradients, particularly in the high affinity binding condition, consistent with our earlier experimental and theoretical observations of dextran and vascular endothelial growth factor (Shirure et al., 2017) (Figure 4c). The relatively flat concentration profiles suggests that elevated interstitial flows (>1 μm/s), as observed in some solid cancers (Munson & Shieh, 2014), would serve to enhance the net rate of EV transport (product of concentration and flow). Bound and free EV concentrations were similar in magnitude, although the bound fraction surpassed free EV concentrations in the high affinity binding condition. Further, high affinity binding resulted in nearly a two-fold increase in total EV concentration (free + bound concentration) compared to intermediate or no binding conditions. These observations highlight the potential biological significance of both free and bound fractions in the interstitium.

We next examined the impact of molecular diffusion by simulating the convective transport into the interstitial channel using a range of molecular diffusivities that included a small molecular weight (~ 40 kDa) dextran ($D = 1.5 \times 10^{-11}$ m^2/s) in a hydrogel, approximate FRAP values of EVs in the laminin-rich ECM ($D = 1.5 \times 10^{-12}$ m^2/s), and an approximate value from an earlier report (Lenzini et al., 2020) that used particle tracking in a different hydrogel ($D = 1.5 \times 10^{-13}$ m^2/s). It is clear from all conditions, particularly those that include binding to the ECM, that diffusion of EVs ($D = 10^{-12}$ m^2/s and smaller) does not impact the bound or free concentrations (1.5×10^{-12} and 1.5×10^{-13} m^2/s curves completely overlap) (Figure 4d). This result can be better understood by examining the relative rates of convection to diffusion using the dimensionless Peclet number (Pe), defined as lv/D, where l is a characteristic length of diffusion (100 μm channel and also similar to the distance between capillaries in vivo), and v is interstitial velocity. For a small dextran (~ 40 kDa), Pe = ~1.4 consistent with both convection and diffusion impacting net transport, which is evident in the shift in the spatial concentration profile when D is further decreased under all binding conditions (Figure 4d). In contrast, for a typical EV (diameter of ~ 100 nm, $D = 1.5 \times 10^{-12}$ m^2/s) under the same conditions, Pe = ~ 33, and thus transport is dominated by convection (diffusion is negligible). This is also evident by the observation that any further decrease in D does not impact the bound or free concentrations of EV (Figure 4d). Finally, disease states of particular interest to nanotherapy formulations, such as cancer, are characterized by elevated interstitial flow (Munson & Shieh, 2014); as such, convection and ECM binding will dominate transport under most conditions.

We next explored the transient nature of the EV free and bound concentration by fixing D and v at our measured and physiologic values of 1.5×10^{-12} m^2/s and 0.5 μm/s, respectively, and examined the spatial concentration profiles at different time points (0-60 min). Spatial gradients of both free and bound EVs are significantly attenuated over 60 min (Figure S6). This observation suggests that steady state spatial concentration profiles are likely flat, and that binding of the EV to the ECM has a significant

20013078, 2023, 4, Downloaded from https://isevjournals.onlinelibrary.wiley.com/doi/10.1002/jev2.12323 by Randy Carney - University Of California - Davis , Wiley Online Library on [29/08/2024]. See the Terms and Conditions (https://onlinelibrary.wiley.com/terms-and-conditions) on Wiley Online Library for rules of use; OA articles are governed by the applicable Creative Commons License

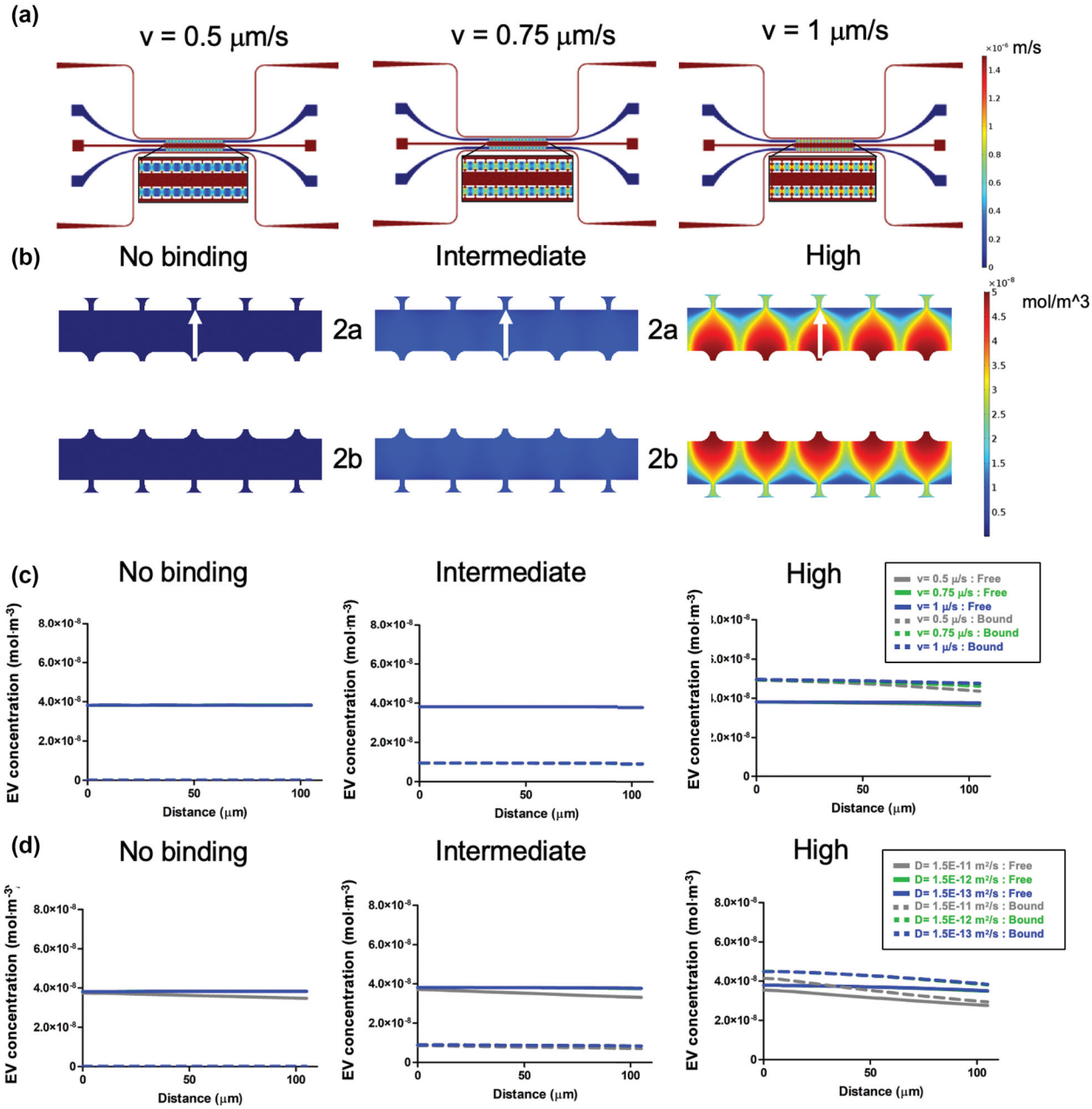

FIGURE 4 Finite element models reveal interstitial accumulation of high affinity binding EVs. (a) A range of physiologically relevant interstitial flow velocities (v, 0.5 – 1 μm/s) were established by varying hydrostatic pressure boundary conditions at port inlets and outlets. (b) Bound EV concentration profiles after T = 30 min with a 0.5 μm/s flow velocity reveal accumulation of bound EVs in compartments 2a and 2b (Fig. S1) as binding affinity increases. Concentration line profiles (white arrows) demonstrated (c) flatter spatial EV concentration profiles with increasing flow velocity as well as higher levels of bound EVs with high affinity binding parameters. (d) Comparing diffusivity of a small molecule dextran with EVs demonstrated differences in spatial profiles, but no significant difference when D < 10^{-12} m^2/s which signifies EV transport is convection-limited.

impact on the absolute concentration of EV. This conclusion is strongly dependent on our boundary condition at the lower pressure side of the interstitial chamber which assumes that all of the EVs are rapidly absorbed (e.g., by a lymphatic or blood vessel).

3.4 | In vitro EV convective transport and binding

We next sought to experimentally observe the transport of EVs under physiologically-relevant conditions consistent with our earlier experimental observations of diffusion and binding and *in silico* predictions (i.e., interstitial flow and a laminin-rich ECM).

20013078, 2023, 4, Downloaded from https://isevjournals.onlinelibrary.wiley.com/doi/10.1002/jev2.12323 by Randy Carney - University Of California - Davis , Wiley Online Library on [29/08/2024]. See the Terms and Conditions (https://onlinelibrary.wiley.com/terms-and-conditions) on Wiley Online Library for rules of use; OA articles are governed by the applicable Creative Commons License

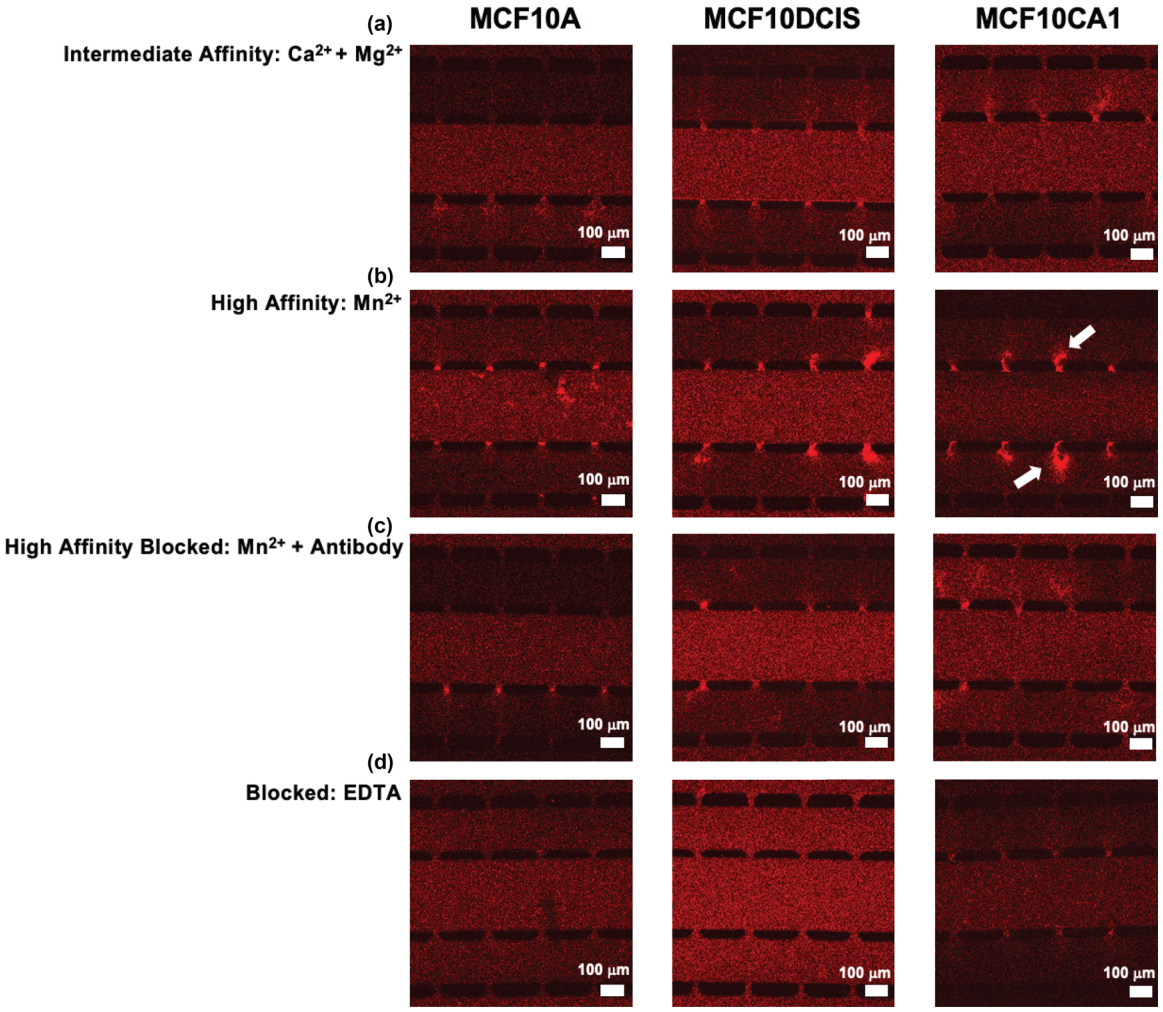

FIGURE 5 Interstitial EV accumulation with increased malignancy and high affinity integrin binding. (a-d) Representative images demonstrated a range of EV binding profiles. Most consistent high binding was observed with MCF10CA1 EVs treated with Mn2+ (b, right column, white arrows) for high affinity binding. Differences in background fluorescent intensity were evident but were normalized for quantitative analysis.

We utilized the same microfluidic device and conditions described for our in silico experiments (Figure S1), and the same ECM and populations of EVs (from the MCF10 series) and experimental conditions from the diffusion-binding experiments.

To validate experimental interstitial flow velocity (i.e., flow through chambers 2a and 2b, Figure S1), fluorescently labeled 40 kDa dextran was added to PBS in chamber 1. Laminin-rich ECM polymerization is anisotropic (Aisenbrey & Murphy, 2020) resulting in spatially heterogeneous hydraulic conductivity and thus interstitial flow. To account for this, we measured the convective transport of the non-binding dextran at each port (Figure S7a), and then used our in silico model to estimate the local permeability and thus interstitial velocity at each pore (Figure S7b,c). The interstitial velocity at most microfluidic device pores fell in a range (0.15-0.75 μm/s; mean = 0.29 μm/s) that was physiologic and consistent with our in silico experiments. Pores outside of this range were not included in the subsequent analysis. To demonstrate that EVs would not be physically trapped within the porous hydrogel, we first introduced fluorescent nanobeads (26 nm and 100 nm diameter) into the central chamber and visualized the convective transport through the pores and into the hydrogel. No evidence of entrapment was observed as evidenced by the near zero spatial gradient within the pore and chamber 2a and 2b for both bead sizes (Figure S8).

Cell line (i.e., malignant potential) and integrin binding state significantly impacted the concentration and spatial distribution of EVs at time 30 min (Figure 5, supplementary videos). Accumulation was most apparent within the first 100 μm of the laminin-rich ECM (Figure 5b; white arrows). Highest EV accumulation was observed with MCF10CA1 EVs treated with $MnCl_2$ (Figure 5b; right column), which is consistent with high binding observed in FRAP and in silico. The addition of EDTA or integrin blocking antibodies (Figure 5c,d) neutralized EV accumulation, particularly with the malignant MCF10CA1 EVs, but also for normal MCF10A and partially malignant MCF10DCIS EVs.

To quantify differences between cell lines and experimental conditions, the fluorescent intensity in the interstitial chamber (chamber 2), after 30 min of convective flow, was first normalized to that in the central chamber (the source, chamber 1). The nor-

20013078, 2023, 4, Downloaded from https://isevjournals.onlinelibrary.wiley.com/doi/10.1002/jev2.12323 by Randy Carney - University Of California - Davis , Wiley Online Library on [29/08/2024]. See the Terms and Conditions (https://onlinelibrary.wiley.com/terms-and-conditions) on Wiley Online Library for rules of use; OA articles are governed by the applicable Creative Commons License

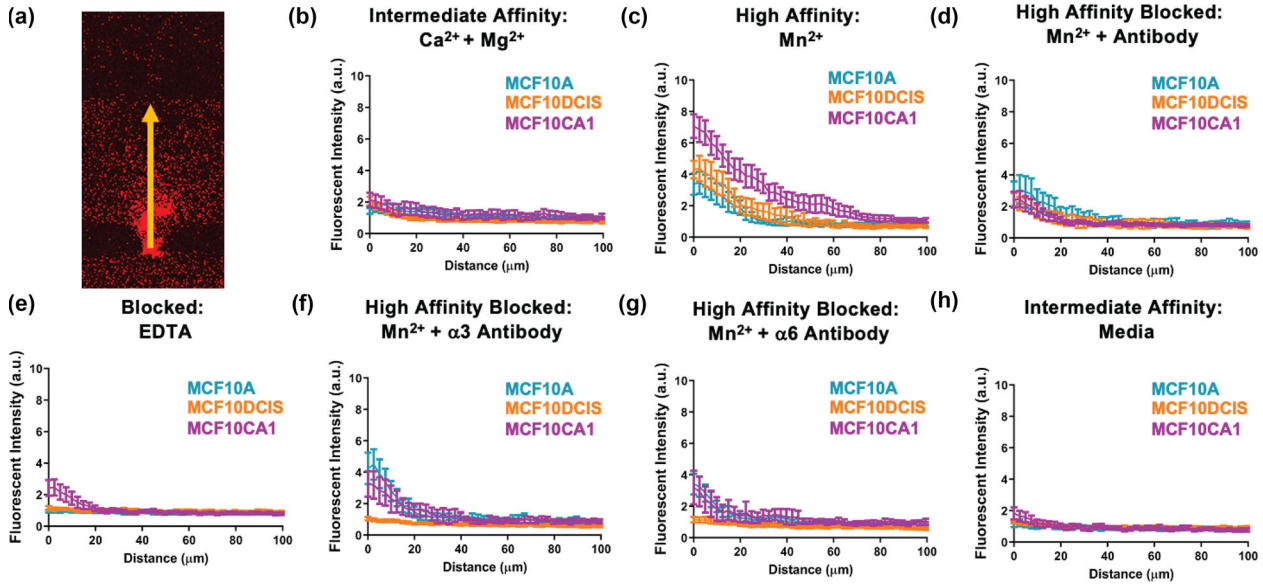

FIGURE 6 EV convective transport is affected by parent cell malignancy and integrin activation state. (a) Line profiles were used to assess EV concentration after T = 30 min of flow. (b-h) Comparisons of concentration profiles by integrin activation state showed highest differences for high affinity MCF10CA1 and MCF10DCIS EV binding. Blocking conditions reduced the formation of spatial gradients. Physiologic binding conditions showed minimal differences between EV conditions. Error bars = 95% CI. n = 2-4 devices per curve (average devices per condition = 3); n = 21-80 ports per curve (average ports per curve = 52).

malized fluorescent intensity was then determined along a linear region across the interstitial chamber (Figure 6a), and resulting curves were averaged (Figure 6b-h). High affinity MCF10CA1 EVs accumulated to eight-fold higher than source concentration followed by MCF10DCIS and MCF10A (Figure 6c). Blocking conditions including an antibody cocktail against laminin binding integrins (Figure 6d), individual integrin blocking antibodies (Figure 6f,g), or EDTA (Figure 6e) dramatically reduced EV accumulation of MCF10CA1 and MCF10DCIS EVs and to a lesser extent MCF10A EVs. Intermediate affinity conditions demonstrated similarly low levels of EV accumulation across cell lines (Figure 6b,h). These results demonstrate that EV binding affinity directly impacts the interstitial spatial distribution and absolute concentration, and that the binding is partially dependent on integrins $\alpha 3$, $\alpha 6$, and $\beta 1$.

It has been previously reported that EVs derived from malignant tumor cells have enhanced rigidity due to lower microenvironmental pH which may impact interstitial transport (Parolini et al., 2009). However, the pore size of our hydrogel as well as that present in most in vivo tissue is much larger than the vast majority of EVs; thus, the rigidity of the EV membrane is not likely to impact interstitial transport and binding. Finally, the increasing impact of integrin blocking antibodies or EDTA with increased malignancy is consistent with the increased presence of integrins with increased malignant potential (Suppl. Tables 2 and 3). Our observation that integrin blocking antibodies significantly impact the spatial distribution of EVs under flow conditions, but did not impact K_d in diffusion only conditions (Figure 3) may be due to the enhanced flux of EVs to the matrix in the presence of flow, or differential sensitives of k_{on} and k_{off} to the presence of flow that render K_d sensitive to integrin blocking under flow conditions [53,] (Almaqwashi et al., 2014). Regardless, this observation highlights the importance of recognizing convection as the dominant mechanism of interstitial EV transport, and its impact on both the total flux of EVs and the ECM binding characteristics.

4 | CONCLUSIONS

EVs can impact biology in myriad ways including critically important phenomena such as cancer metastasis. In addition, the inherent qualities of EVs provide an exciting and flexible new platform for novel nanotherapeutics. Progress has been slowed by a limited understanding of the fundamental mechanisms of transport in tissue spaces, which will dictate the spatial distribution and concentration. Using a combination of technologies, we demonstrate that diffusion of EVs under physiological conditions in the interstitium is negligible, and that transport, and thus the spatial distribution of bound and free EVs, is dominated by interstitial flow (convection) and binding to the ECM. The EVs, derived from a cell line series of progressively increasing malignancy, express laminin-binding integrins ($\alpha 3$, $\alpha 6$, and $\beta 1$) that increase with malignant potential and contribute to the spatial distribution and concentration of EVs. These results provide a paradigm shift in our understanding of the mechanisms that control interstitial transport of EVs and should impact the design and strategies to deliver nanotherapeutics broadly.

20013078, 2023, 4, Downloaded from https://isevjournals.onlinelibrary.wiley.com/doi/10.1002/jev2.12323 by Randy Carney - University Of California - Davis , Wiley Online Library on [29/08/2024]. See the Terms and Conditions (https://onlinelibrary.wiley.com/terms-and-conditions) on Wiley Online Library for rules of use; OA articles are governed by the applicable Creative Commons License

AUTHOR CONTRIBUTION

Peter A. Sariano: Conceptualization; Data curation; Formal analysis; Writing original draft. **Rachel R. Mizenko**: Conceptualization; Data curation; Formal analysis; Writing – review & editing. **Venktesh S. Shirure**: Data curation; Formal analysis; Writing – review & editing. **Abigail K. Brandt**: Data curation; Formal analysis; Writing – review & editing. **Bryan B. Nguyen**: Data curation; Formal analysis.**Cem Nesiri**: Data curation; Formal analysis; Writing – review & editing. **Bhupinder S. Shergill**: Data curation; Formal analysis; Writing – review & editing. **Terza Brostoff**: Data curation; Formal analysis. **David M. Rocke**: Formal analysis; Writing – review & editing.**Alexander Borowsky**: Conceptualization. **Randy Carney**: Conceptualization; Formal analysis; Writing – review & editing. **Steven George**: Conceptualization; Formal analysis; Writing – original draft, review & editing.

ACKNOWLEDGEMENTS

This work supported, in part, by an NSF Graduate Research Fellowship (PAS), the ARCS Foundation Scholar Award (PAS), grants from the National Institutes of Health (UH3 HL141800, R01 EB030410, R21 AI161041, R01 CA241666, F31 NS120590), and funds from the Department of Biomedical Engineering and the College of Engineering at the University of California, Davis.

CONFLICT OF INTEREST

There are no conflicts of interest to declare.

ORCID

Randy P. Carney https://orcid.org/0000-0001-8193-1664
Steven C. George https://orcid.org/0000-0003-2263-1914

REFERENCES

Aisenbrey, E. A., & Murphy, W. L. (2020). Synthetic alternatives to Matrigel. *Nature Reviews Materials*, *5*, 539–551.

Almaqwashi, A. A., Paramanathan, T., Lincoln, P., Rouzina, I., Westerlund, F., & Williams, M. C. (2014). Strong DNA deformation required for extremely slow DNA threading intercalation by a binuclear ruthenium complex. *Nucleic Acids Research*, *42*, 11634–11641.

Aumailley, M. (2013). The laminin family. *Cell Adhesion & Migration*, *7*, 48–55.

Becker, A., Thakur, B. K., Weiss, J. M., Kim, H. S., Peinado, H., & Lyden, D. (2016). Extracellular vesicles in cancer: Cell-to-cell mediators of metastasis. *Cancer Cell*, *30*, 836–848. Preprint at https://doi.org/10.1016/j.ccell.2016.10.009

Behbod, F., Kittrell, F. S., Lamarca, H., Edwards, D., Kerbawy, S., Heestand, J. C., Young, E., Mukhopadhyay, P., Yeh, H.-W., Allred, D. C., Hu, M., Polyak, K., Rosen, J. M., & Medina, D. (2009). An intraductal human-in-mouse transplantation model mimics the subtypes of ductal carcinoma in situ. *Breast Cancer Res* **11**, *R66*. https://doi.org/10.1186/bcr2358

Bessette, D. C., Tilch, E., Seidens, T., Quinn, M. C. J., Wiegmans, A. P., Shi, W., Cocciardi, S., Mccart-Reed, A., Saunus, J. M., Simpson, P. T., Grimmond, S. M., Lakhani, S. R., Khanna, K. K., Waddell, N., Al-Ejeh, F., & Chenevix-Trench, G. (2015). Using the MCF10A/MCF10CA1a breast cancer progression cell line model to investigate the effect of active, mutant forms of EGFR in breast cancer development and treatment using gefitinib. *PLoS ONE*, *10*, e0125232.

Bonsergent, E., Grisard, E., Buchrieser, J., Schwartz, O., Théry, C., & Lavieu, G. (2021). Quantitative characterization of extracellular vesicle uptake and content delivery within mammalian cells. *Nature Communications*, *12*, 1864.

Brown, M., Johnson, L. A., Leone, D. A., Majek, P., Vaahtomeri, K., Senfter, D., Bukosza, N., Schachner, H., Asfour, G., Langer, B., Hauschild, R., Parapatics, K., Hong, Y.-K., Bennett, K. L., Kain, R., Detmar, M., Sixt, M., Jackson, D. G., & Kerjaschki, D. (2018). Lymphatic exosomes promote dendritic cell migration along guidance cues. *Journal of Cell Biology*, *217*, 2205–2221.

Chary, S. R., & Jain, R. K. (1989). Direct measurement of interstitial convection and diffusion of albumin in normal and neoplastic tissues by fluorescence photobleaching. *Proceedings of the National Academy of Sciences of the United States of America*, *86*, 5385–5389.

Chin, A. R., Yan, W., Cao, M., Liu, X., & Wang, S. E. (2018). Polarized secretion of extracellular vesicles by mammary epithelia. *Journal of Mammary Gland Biology and Neoplasia*, *23*, 165–176.

Cho, H., Kim, H.-Y., Kang, J. Y., & Kim, T. S. (2007). How the capillary burst microvalve works. *Journal of Colloid & Interface Science*, *306*, 379–385.

Dolo, V., Ginestra, A., Cassarà, D., Violini, S., Lucania, G., Torrisi, M. R., Nagase, H., Canevari, S., Pavan, A., & Vittorelli, M. L. (1998). Selective localization of matrix metalloproteinase 9, beta1 integrins, and human lymphocyte antigen class I molecules on membrane vesicles shed by 8701-BC breast carcinoma cells. *Cancer Research*, *58*, 4468–4474.

Elsharkasy, O. M., Nordin, J. Z., Hagey, D. W., De Jong, O. G., Schiffelers, R. M., Andaloussi, S. E., & Vader, P. (2020). Extracellular vesicles as drug delivery systems: Why and how? *Advanced Drug Delivery Reviews*, *159*, 332–343.

Espina, V., Mariani, B. D., Gallagher, R. I., Tran, K., Banks, S., Wiedemann, J., Huryk, H., Mueller, C., Adamo, L., Deng, J., Petricoin, E. F., Pastore, L., Zaman, S., Menezes, G., Mize, J., Johal, J., Edmiston, K., & Liotta, L. A. (2010). Malignant precursor cells pre-exist in human breast DCIS and require autophagy for survival. *PLoS ONE*, *5*, e10240.

Gangoda, L., Liem, M., Ang, C.-S., Keerthikumar, S., Adda, C. G., Parker, B. S., & Mathivanan, S. (2017). Proteomic profiling of exosomes secreted by breast cancer cells with varying metastatic potential. *Proteomics*, *17*, 1600370.

Ganguly, K. K., Pal, S., Moulik, S., & Chatterjee, A. (2013). Integrins and metastasis. *Cell Adhesion & Migration*, *7*, 251–261.

Garcia-Martin, R., Brandao, B. B., Thomou, T., Altindis, E., & Kahn, C. R. (2022). Tissue differences in the exosomal/small extracellular vesicle proteome and their potential as indicators of altered tissue metabolism. *Cell Reports*, *38*, 110277.

Genschmer, K. R., Russell, D. W., Lal, C., Szul, T., Bratcher, P. E., Noerager, B. D., Abdul Roda, M., Xu, X., Rezonzew, G., Viera, L., Dobosh, B. S., Margaroli, C., Abdalla, T. H., King, R. W., Mcnicholas, C. M., Wells, J. M., Dransfield, M. T., Tirouvanziam, R., Gaggar, A., & Blalock, J. E. (2019). Activated PMN exosomes: Pathogenic entities causing matrix destruction and disease in the lung. *Cell*, *176*, 113–126. e15.

George, S. C., Babb, A. L., Deffebach, M. E., & Hlastala, M. P. (1996). Diffusion of nonelectrolytes in the canine trachea: Effect of tight junction. *Journal of Applied Physiology*, *80*, 1687–1695.

20013078, 2023, 4, Downloaded from https://isevjournals.onlinelibrary.wiley.com/doi/10.1002/jev2.12323 by Randy Carney - University Of California - Davis , Wiley Online Library on [29/08/2024]. See the Terms and Conditions (https://onlinelibrary.wiley.com/terms-and-conditions) on Wiley Online Library for rules of use; OA articles are governed by the applicable Creative Commons License

Hosseini, R., Asef-Kabiri, L., Yousefi, H., Sarvnaz, H., Salehi, M., Akbari, M. E., & Eskandari, N. (2021). The roles of tumor-derived exosomes in altered differentiation, maturation and function of dendritic cells. *Molecular Cancer*, *20*, 1–17.

Huang, J., Ding, Z., Luo, Q., & Xu, W. (2019). Cancer cell-derived exosomes promote cell proliferation and inhibit cell apoptosis of both normal lung fibroblasts and non-small cell lung cancer cell through delivering alpha-smooth muscle actin. *American Journal of Translational Research*, *11*, 1711.

Huleihel, L., Hussey, G. S., Naranjo, J. D., Zhang, L., Dziki, J. L., Turner, N. J., Stolz, D. B., & Badylak, S. F. (2016). Matrix-bound nanovesicles within ECM bioscaffolds. *Science Advances*, *2*, 00–00.

Hwang, P. Y., Brenot, A., King, A. C., Longmore, G. D., & George, S. C. (2019). Randomly distributed K14(+) breast tumor cells polarize to the leading edge and guide collective migration in response to chemical and mechanical environmental cues. *Cancer Research*, *79*, 1899–1912.

Imbalzano, K. M., Tatarkova, I., Imbalzano, A. N., & Nickerson, J. A. (2009). Increasingly transformed MCF-10A cells have a progressively tumor-like phenotype in three-dimensional basement membrane culture. *Cancer Cell International*, *9*, 1–11.

Jimenez, L., Yu, H., Mckenzie, A. J., Franklin, J. L., Patton, J. G., Liu, Q., & Weaver, A. M. (2019). Quantitative proteomic analysis of small and large extracellular vesicles (EVs) reveals enrichment of adhesion proteins in small EVs. *Journal of Proteome Research*, *18*, 947–959.

Jordan, K. R., Hall, J. K., Schedin, T., Borakove, M., Xian, J. J., Dzieciatkowska, M., Lyons, T. R., Schedin, P., Hansen, K. C., & Borges, V. F. (2020). Extracellular vesicles from young women's breast cancer patients drive increased invasion of non-malignant cells via the Focal Adhesion Kinase pathway: A proteomic approach. *Breast Cancer Res* **22**, 128, https://doi.org/10.1186/s13058-020-01363-x

Kilinc, S., Paisner, R., Camarda, R., Gupta, S., Momcilovic, O., Kohnz, R. A., Avsaroglu, B., L'etoile, N. D., Perera, R. M., Nomura, D. K., & Goga, A. (2021). Oncogene-regulated release of extracellular vesicles. *Developmental Cell*, *56*, 1989–2006. e6.

Kriebel, P. W., Majumdar, R., Jenkins, L. M., Senoo, H., Wang, W., Ammu, S., Chen, S., Narayan, K., Iijima, M., & Parent, C. A. (2018). Extracellular vesicles direct migration by synthesizing and releasing chemotactic signals. *Journal of Cell Biology*, *217*, 2891–2910.

Lenzini, S., Bargi, R., Chung, G., & Shin, J.-W. (2020). Matrix mechanics and water permeation regulate extracellular vesicle transport. *Nature Nanotechnology*, *15*, 217–223.

Lo Cicero, A., Majkowska, I., Nagase, H., Di Liegro, I., & Troeberg, L. (2012). Microvesicles shed by oligodendroglioma cells and rheumatoid synovial fibroblasts contain aggrecanase activity. *Matrix Biology*, *31–20*, 229–233.

Loh, Q. L., & Choong, C. (2013). Three-dimensional scaffolds for tissue engineering applications: Role of porosity and pore size.

Matsumoto, Y., Kano, M., Murakami, K., Toyozumi, T., Suito, H., Takahashi, M., Sekino, N., Shiraishi, T., Kamata, T., Ryuzaki, T., Hirasawa, S., Kinoshita, K., & Matsubara, H. (2020). Tumor-derived exosomes influence the cell cycle and cell migration of human esophageal cancer cell lines. *Cancer Science*, *111*, 4348–4358.

Mizenko, R. R., Brostoff, T., Rojalin, T., Koster, H. J., Swindell, H. S., Leiserowitz, G. S., Wang, A., & Carney, R. P. (2021). Tetraspanins are unevenly distributed across single extracellular vesicles and bias sensitivity to multiplexed cancer biomarkers. *Journal of Nanobiotechnology*, *19*, 250.

Morales-Kastresana, A., Telford, B., Musich, T. A., Mckinnon, K., Clayborne, C., Braig, Z., Rosner, A., Demberg, T., Watson, D. C., Karpova, T. S., Freeman, G. J., Dekruyff, R. H., Pavlakis, G. N., Terabe, M., Robert-Guroff, M., Berzofsky, J. A., & Jones, J. C. (2017). Labeling extracellular vesicles for nanoscale flow cytometry. *Scientific Reports*, *7*, 1–10.

Moya, M. L., Hsu, Y.-H., Lee, A. P., Hughes, C. C. W., & George, S. C. (2013). In vitro perfused human capillary networks. *Tissue Engineering Part C: Methods*, *19*, 730–737.

Munson, J., & Shieh, A. (2014). Interstitial fluid flow in cancer: Implications for disease progression and treatment. *Cancer Management and Research*, *6*, 317–328.

Parolini, I., Federici, C., Raggi, C., Lugini, L., Palleschi, S., De Milito, A., Coscia, C., Iessi, E., Logozzi, M., Molinari, A., Colone, M., Tatti, M., Sargiacomo, M., & Fais, S. (2009). Microenvironmental pH is a key factor for exosome traffic in tumor cells. *Journal of Biological Chemistry*, *284*, 34211–34222.

Provenzano, P. P., Eliceiri, K. W., Campbell, J. M., Inman, D. R., White, J. G., & Keely, P. J. (2006). Collagen reorganization at the tumor-stromal interface facilitates local invasion. *BMC Medicine*, *4*, 1–15.

Raviraj, V., Fok, S., Zhao, J., Chien, H.-Y., Lyons, J. G., Thompson, E. W., & Soon, L. (2012). Regulation of ROCK1 via Notch1 during breast cancer cell migration into dense matrices. *BMC Cell Biology*, *13*, 1–17.

Risha, Y., Minic, Z., Ghobadloo, S. M., & Berezovski, M. V. (2020). The proteomic analysis of breast cell line exosomes reveals disease patterns and potential biomarkers. *Sci Rep* **10**, 13572. https://doi.org/10.1038/s41598-020-70393-4

Rossi, C., & Bianchi, E. (1961). Diffusion of small molecules. *Nature*, *189*, 822–824.

Shirure, V. S., Lezia, A., Tao, A., Alonzo, L. F., & George, S. C. (2017). Low levels of physiological interstitial flow eliminate morphogen gradients and guide angiogenesis. *Angiogenesis*, *20*, 493–504. https://www.ncbi.nlm.nih.gov/pubmed/28608153

Sprague, B. L., Pego, R. L., Stavreva, D. A., & Mcnally, J. G. (2004). Analysis of binding reactions by fluorescence recovery after photobleaching. *Biophysical Journal*, *86*, 3473–3495.

Sung, B. H., Ketova, T., Hoshino, D., Zijlstra, A., & Weaver, A. M. (2015). Directional cell movement through tissues is controlled by exosome secretion. *Nature Communications*, *6*, 7164.

Sung, B. H., & Weaver, A. M. (2017). Exosome secretion promotes chemotaxis of cancer cells. *Cell Adhesion & Migration*, *11*, 187–195.

Swabb, E. A., Wei, J., & Gullino, P. M. (1974). Diffusion and convection in normal and neoplastic tissues. *Cancer Research*, *34*, 2814–2822.

Swartz, M. A., & Lund, A. W. (2012). Lymphatic and interstitial flow in the tumour microenvironment: Linking mechanobiology with immunity. *Nature Reviews Cancer*, *12*, 210–219.

Takada, Y., Ye, X., & Simon, S. (2007). The integrins *Genome Biol*, *8*, 215.

Unruh, J. Stowers ImageJ Plugins: Jay_Plugins.jar.

Vu, L. T., Peng, B., Zhang, D. X., Ma, V., Mathey-Andrews, C. A., Lam, C. K., Kiomourtzis, T., Jin, J., Mcreynolds, L., Huang, L., Grimson, A., Cho, W. C., Lieberman, J., & Le, M. T. (2019). Tumor-secreted extracellular vesicles promote the activation of cancer-associated fibroblasts via the transfer of microRNA-125b. *Journal of Extracellular Vesicles*, *8*, 1599680.

Wang, L., Johnson, J. A., Zhang, Q., & Beahm, E. K. (2013). Combining decellularized human adipose tissue extracellular matrix and adipose-derived stem cells for adipose tissue engineering. *Acta Biomaterialia*, *9*, 8921–8931.

Wang, Y., Yan, J., & Goult, B. T. (2019). Force-dependent binding constants. *Biochemistry*, *58*, 4696–4709.

Whiteside, T. L. (2016). Exosomes and tumor-mediated immune suppression. *Journal of Clinical Investigation*, *126*, 1216–1223.

You, Y., Shan, Y., Chen, J., Yue, H., You, B., Shi, S., Li, X., & Cao, X. (2015). Matrix metalloproteinase 13-containing exosomes promote nasopharyngeal carcinoma metastasis. *Cancer Science*, *106*, 1669–1677.

Yuan, P., Ding, L., Chen, H., Wang, Y., Li, C., Zhao, S., Yang, X., Ma, Y., Zhu, J., Qi, X., Zhang, Y., Xia, X., & Zheng, J. C. (2021). Neural stem cell-derived exosomes regulate neural stem cell differentiation through miR-9-Hes1 axis. *Frontiers in Cell and Developmental Biology*, *9*, 1181.

20013078, 2023, 4, Downloaded from https://isevjournals.onlinelibrary.wiley.com/doi/10.1002/jev2.12323 by Randy Carney - University Of California - Davis , Wiley Online Library on [29/08/2024]. See the Terms and Conditions (https://onlinelibrary.wiley.com/terms-and-conditions) on Wiley Online Library for rules of use; OA articles are governed by the applicable Creative Commons License

Zaman, M. H., Trapani, L. M., Sieminski, A. L., Mackellar, D., Gong, H., Kamm, R. D., Wells, A., Lauffenburger, D. A., & Matsudaira, P. (2006). Migration of tumor cells in 3D matrices is governed by matrix stiffness along with cell-matrix adhesion and proteolysis. *Proceedings of the National Academy of Sciences*, *103*, 10889–10894.

SUPPORTING INFORMATION

Additional supporting information can be found online in the Supporting Information section at the end of this article.

How to cite this article: Sariano, P. A., Mizenko, R. R., Shirure, V. S., Brandt, A. K., Nguyen, B. B., Nesiri, C., Shergill, B. S., Brostoff, T., Rocke, D. M., Borowsky, A. D., Carney, R. P., & George, S. C. (2023). Convection and extracellular matrix binding control interstitial transport of extracellular vesicles. *Journal of Extracellular Vesicles*, *12,* e12323. https://doi.org/10.1002/jev2.12323

20013078, 2023, 4, Downloaded from https://isevjournals.onlinelibrary.wiley.com/doi/10.1002/jev2.12323 by Randy Carney - University Of California - Davis , Wiley Online Library on [29/08/2024]. See the Terms and Conditions (https://onlinelibrary.wiley.com/terms-and-conditions) on Wiley Online Library for rules of use; OA articles are governed by the applicable Creative Commons License